

Article

Effect of Channel Diameter on the Combustion and Thermal Behavior of a Hydrogen/Air Premixed Flame in a Swirl Micro-Combustor

Xiao Yang ^{1,2} , Zhihong He ², Lei Zhao ^{1,2}, Shikui Dong ^{1,2,*}  and Heping Tan ^{1,2}

¹ Key laboratory of Aerospace Thermophysics, Ministry of Industry and Information Technology, School of Energy Science and Engineering, Harbin Institute of Technology, Harbin 150001, China; yangxiaohit@163.com (X.Y.); zhaoleihit@163.com (L.Z.); tanheping@hit.edu.cn (H.T.)

² School of Energy Science and Engineering, Harbin Institute of Technology, Harbin 150001, China; zhihong_he@hit.edu.cn

* Correspondence: dongsk@hit.edu.cn

Received: 5 September 2019; Accepted: 8 October 2019; Published: 10 October 2019



Abstract: Improving the flame stability and thermal behavior of the micro-combustor (MC) are major challenges in microscale combustion. In this paper, the micro combustions of an H₂/air premixed flame in a swirl MC with various channel diameters ($D_{in} = 2, 3, 4$ mm) were analyzed based on an established three-dimensional numerical model. The effects of hydrogen mass flow rate, thermal conductivity of walls, and the preferential transport of species were investigated. The results indicated that the flame type was characterized by the presence of two recirculation zones. The flame was anchored by the recirculation zones, and the anchoring location of the flame root was the starting position of the recirculation zones. The recirculation zones had a larger distribution of local equivalence ratio, especially in the proximity of the flame root, indicating the formation of a radical pool. The combustion efficiency increased with an increasing D_{in} due to the longer residence time of the reactants. Furthermore, the MC with $D_{in} = 2$ mm obtained the highest outer wall temperature distribution. However, the MC with $D_{in} = 4$ mm had a better uniformity of outer wall temperature and large emitter efficiency due to the larger radiation surface. An increase in thermal conductivity boosts the thermal performance of combustion efficiency, emitter efficiency, and wall temperature uniformity. But there is a critical point of thermal conductivity that can increase the thermal performance. The above results can offer us significant guidance for designing MC with high thermal performance.

Keywords: micro combustion; hydrogen; swirl micro-combustor; channel diameter; flame anchoring

1. Introduction

With the development of micro electro-mechanical systems (MEMS), micro power generators with high energy density and low weight are pressingly required [1–4]. The high energy density of hydrocarbon fuels offers great potential for micro combustion-based micro power generators, for instance, micro gas turbine [5,6], micro thermophotovoltaic [7–11], and micro thermoelectric [12–14] systems. However, there are some challenges in obtaining a stable flame and better thermal performance in micro-combustors (MCs). The short residence time and large heat loss on account of the small size and large surface-area-to-volume ratio are the main challenges of micro combustion [15], which can result in incomplete combustion and an unstable flame.

As regards micro combustion, heat recirculation is the most widely used method to stabilize the flame. Wan et al. [16,17] found that the bluff-body in MCs markedly improves the flame stability owing to the flow recirculation zone behind the bluff-body and the upstream heat transfer through the wall,

and the large flame strain rate results in flame extinguishment. For the hydrogen/air premixed flame, a study by Bagheri et al. [18] examined how bluff-body shapes affect flame characteristics. As for the micro-flameless combustion of a methane/air mixture, Hosseini and Wahid [19] used the bluff-body to improve micro-flameless combustion stability. A new configuration of a Swiss-roll combustor is a favorable technique to stabilize the flame through recirculating heat from high-temperature gas [20]. The flame characteristics of Swiss-roll combustors with various channel widths were investigated by Kim et al. [21]. They found that Swiss-roll combustors can establish self-sustaining flames where the channel widths are less than the quenching distance. In addition, filling or partially filling the porous media in the MC can be used to strengthen heat transfer from high-temperature gas to low-temperature gas, leading to more heat recirculation. A planar MC partially filled with nickel foam for flame stability was examined by Wang et al. [22]. The porous media reduces the heat loss and the flame temperature in the MC increases on account of the heat recirculation in porous media. Li et al. [23] found that the flame temperature and temperature non-uniformity are lowered, while the wall temperature is increased in a porous MC. Marbach et al. [24] utilized a porous media surface to stabilize the flame in a cylindrically recuperative MC with silicon-carbide-coated carbon foam. Mikami et al. [25] used wire mesh for enhancing heat transfer in meso-scale tubes, and the wire mesh helped to create a stable flame.

For the application of a micro thermophotovoltaic power generator, many studies are working to improve the thermal performance of MCs in order to further increase the energy output power or efficiency. It is confirmed that heat recirculation is a significant method. Recuperators, such as quartz glass cover, can reuse the exhaust gas energy, which is able to markedly improve the outer wall temperature [26]. Tang et al. [27] designed and fabricated a heat recirculation MC for the application of micro thermophotovoltaic power generator. Experimental data indicated that the radiation efficiency was markedly improved due to the heat recirculation, and the blowout limit in the heat recirculation MC was larger compared with the straight-channel MC. Alipoor and Saidi [28] developed a U-shaped micro tube combustor inside rectangular walls. Secondary flows can better preheat the incoming cold reactants, which enlarges the flammability limits. They have obtained an emitter efficiency of 41.1% and total energy conversion efficiency of 6.3%. Chou et al. [29] employed the porous media to increase the wall temperature and radiation energy in a cylindrical tube combustor. Furthermore, it is effective to optimize the MC structures. Akhtar et al. [30] revealed that a curved channel can significantly improve the overall energy conversion efficiency by about 7.84%, while the flame flashback is more likely to occur. In order to acquire higher energy output, Yang et al. [31] proposed a converging–diverging channel MC for micro thermophotovoltaic power generator. They pointed out that the flow disturbance caused by the converging–diverging channel improves the heat transfer between the gas and the solid wall. Parallel separating plates were employed by Tang et al. [32] in a planar MC for improving the thermal performance, resulting in an increase in the wall temperature of more than 100 K. Moreover, Amani et al. [33] used hydrogen addition to enhance the thermal performance of the MC combined with baffles and bluff-bodies for a premixed methane–air flame. Hydrogen addition can also raise the combustion reaction rate and flame stability of premixed methane/air [34]. As regards the micro thermophotovoltaic system, Yang et al. [35] used GaSb PV cells for this system to obtain a 4.4 W electrical power output with an overall efficiency of 3.48%. Lee et al. [36] employed an ammonia–hydrogen mixture as fuel for the application of micro thermophotovoltaic system, and an energy output power of 5.2 W and an overall efficiency of 2.1% were obtained. Nadimi and Jafarmadar [37] utilized the internal micro-fin that was placed inside an MC to improve the efficiency. They found a maximum total efficiency of 8.9% when the radiant efficiency of the MC was 58%. Gentillon et al. [38] experimentally investigated a porous media combustion-based thermophotovoltaic system, and the electrical power of 1 W was produced and the corresponding total efficiency was 0.071%.

Recently, we developed a swirl MC [39] fueled by hydrogen/air based on a swirl-stabilized flame configuration, and the combustion and thermal performances under premixed modes and non-premixed modes were compared and analyzed. Indeed, the analysis revealed that the formation of an inner recirculation zone and corner recirculation zone in the chamber were major contributing factors

in the flame's stabilization. The channel diameter played a key role in the formation of the recirculation zones in the chamber. In addition, the energy output performance of the MC was also affected by the channel diameter. Thus, in the present work, the influence of channel diameter on combustion and thermal performance was investigated based on three-dimensional numerical simulations. In addition, the performance of an MC with different thermal conductivities of solid walls was also investigated. The results of this work offer a number of valuable guidelines for the design and optimization of MCs.

2. Methodology

2.1. Physical Model

The swirl MC configuration is exhibited in Figure 1. Except for the channel diameter D_{in} , other structural parameters were kept the same. The thickness of the wall (δ) was 0.5 mm. The lengths of entrance section (L_1) and combustion chamber (L_2) were 2 mm and 18 mm, respectively. An axial annular swirl generator was placed at the entrance section with 6 blades, each of which had a discharge angle of 45° . In addition, the inner and outer diameters of the swirler had values of 0.6 mm and 1.0 mm, respectively. Based on the swirl number calculation of the axial annular swirl generator [40], the swirl number was approximately 0.82 in this combustor. Moreover, it should be emphasized that this exact swirler geometry was captured in the numerical modelling and the swirl number did not vary with the inlet mass flow rate. The combustor was made of silicon carbide, which had thermal conductivity and emissivity values of 32.8 W/m·K and 0.9, respectively. Detailed geometrical parameters are shown in Figure 1.

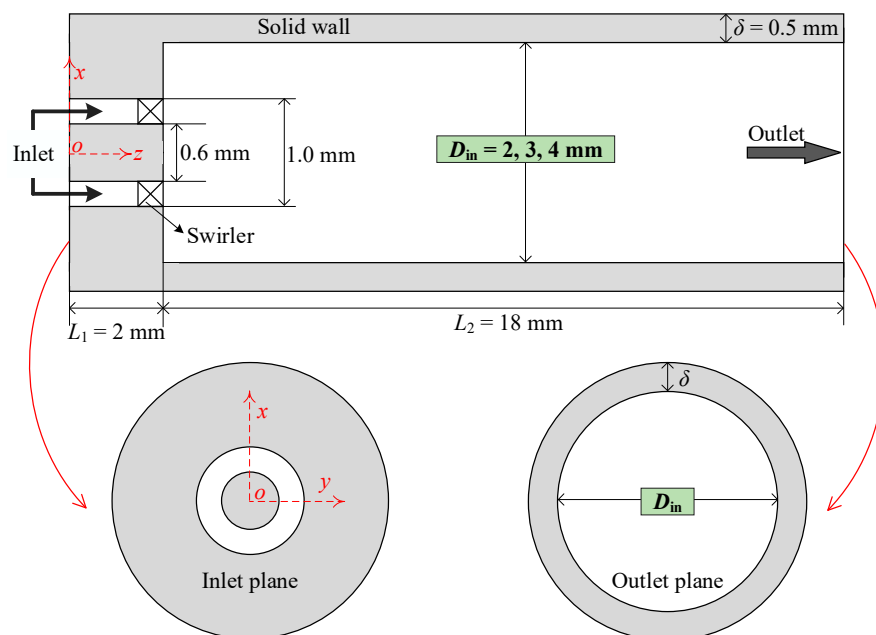


Figure 1. Schematic of the swirl micro-combustor (MC) configuration.

2.2. Computational Models

A three-dimensional, steady-state numerical modelling was built using the computational fluid dynamics software Fluent 15.0. It is true that the Navier–Stokes equation could be utilized for this study in that the Knudsen number of the gas mixture was much smaller than 0.001 [41]. For the purpose of simplifying the mathematical model, the Dufour effects, gas radiation, surface reactions, and work done by pressure and viscous forces were neglected [42,43]. The realizable $k-\varepsilon$ turbulence model [16,44] was applied for solving the turbulent flow. The basic governing equations about continuity, momentum, energy, and spaces conservation are shown below:

Continuity:

$$\frac{\partial \rho}{\partial t} + \nabla \cdot (\rho \vec{v}) = 0 \quad (1)$$

Momentum:

$$\frac{\partial}{\partial t}(\rho \vec{v}) + \nabla \cdot (\rho \vec{v} \vec{v}) = -\nabla p + \nabla \cdot \bar{\tau} \quad (2)$$

Energy:

$$\frac{\partial}{\partial t}(\rho E) + \nabla \cdot [\vec{v}(\rho E + p)] = \nabla \cdot \left[k_{eff} \nabla T - \sum_i h_i \vec{J}_i + (\bar{\tau} \cdot \vec{v}) \right] + S_h \quad (3)$$

$$\frac{\partial}{\partial t}(\rho_s c_s T) + \nabla \cdot (k_s \cdot \nabla T) = 0 \quad (4)$$

Species:

$$\frac{\partial}{\partial t}(\rho Y_i) + \nabla \cdot (\rho \vec{v} Y_i) = -\nabla \cdot \vec{J}_i + R_i \quad (5)$$

where ρ , \vec{v} , and p are the gas density, velocity vector, and gas static pressure, respectively; $\bar{\tau}$ is the stress tensor; E , k_{eff} , and T are the total energy, effective conductivity, and temperature, respectively; h_i and \vec{J}_i are the enthalpy and diffusion flux of species i , respectively; S_h is the fluid enthalpy source; k_s , ρ_s , and c_s are the thermal conductivity, density, and specific heat of the solid phase; Y_i and R_i are the mass fraction of species i and the net rate of production of species i , respectively.

With regards to the combustion model, the detailed H₂/air chemical reaction mechanism with 9 species and 19 reversible reactions [31] was implemented in this numerical modelling. The eddy dissipation conception (EDC) model is devoted to solving the turbulence–chemistry interaction. In addition, the Soret effect is much smaller than the Fickian diffusion, and the Soret effect has negligible influence on the numerical results based on our previous study [39]. Accordingly, only the mass diffusion was considered in this study. The ideal gas law was used to calculate the density of the mixture, while the mass weighted mixing law was used for the specific heat, thermal conductivity, and viscosity of the mixture, as shown below.

Specific heat:

$$c_p = \sum_i Y_i c_{p,i}, \text{ with } c_{p,i} = \frac{1}{2} \frac{R}{M_{w,i}} (f_i + 2) \quad (6)$$

Thermal conductivity:

$$k = \sum_i Y_i k_i, \text{ with } k_i = \frac{15}{4} \frac{R}{M_{w,i}} \mu_i \left[\frac{4}{15} \frac{c_{p,i} M_{w,i}}{R} + \frac{1}{3} \right] \quad (7)$$

Viscosity:

$$\mu = \sum_i Y_i \mu_i, \text{ with } \mu_i = 2.67 \times 10^{-6} \frac{\sqrt{M_{w,i} T}}{\sigma^2 \Omega_\mu} \quad (8)$$

where $M_{w,i}$ and f_i are the molecular weight and the number of modes of energy storage (degrees of freedom) for the species i , respectively; R is the universal gas constant; and M_w is the molecular weight.

For the inlet, both velocity and composition are considered to be uniform, and the temperature of it is 300 K. The pressure-outlet boundary condition is utilized for the outlet. The gas–solid interface uses non-slip and zero diffusive flux species boundary conditions. The energy output Q_0 from the MC outer wall via natural convection and thermal radiation is expressed by:

$$Q_0 = h_0 A (T_w - T_0) + \varepsilon \sigma A (T_w^4 - T_0^4) \quad (9)$$

where h_0 and T_0 are the natural convection coefficient and ambient temperature, which are 10 W/(m²·K) and 300 K [45], respectively; A and T_w are the surface area and temperature of the outer wall,

respectively; ε and σ are the wall emissivity and Stephen–Boltzmann constant, which are 0.9 and $5.67 \times 10^{-8} \text{ W}/(\text{m}^2 \cdot \text{K}^4)$.

The second order upwind scheme and the SIMPLE scheme were utilized for discretizing the equations and the pressure–velocity coupling. The simulation results were considered to be converged when the residual of the energy equation was not greater than 10^{-6} and the residuals of other equations were not greater than 10^{-3} . Furthermore, the grid independence was checked in a swirl MC with $D_{\text{in}} = 2 \text{ mm}$ under three mesh cells of 534,200; 1,245,800; and 1,748,500 cells in the case of $m_{\text{H}_2} = 2.16 \text{ g/h}$ and $\Phi = 1.0$. The temperatures of the centerline and outer walls are depicted in Figure 2. As it can be observed from the graph, the differences in the centerline wall temperature were small, at the same time, the outer wall temperature profiles of the three cases almost overlapped. In addition, the difference in the standard deviation of the outer wall temperature was really small. Thus, the mesh with the cell number of 1,245,800 was selected as the preferable grid structure in this study. The numerical modelling established in this study was the same as in the literature [37,39], of which the results were confirmed to be accurate and effective in simulating the premixed H_2/air combustion in micro-combustors.

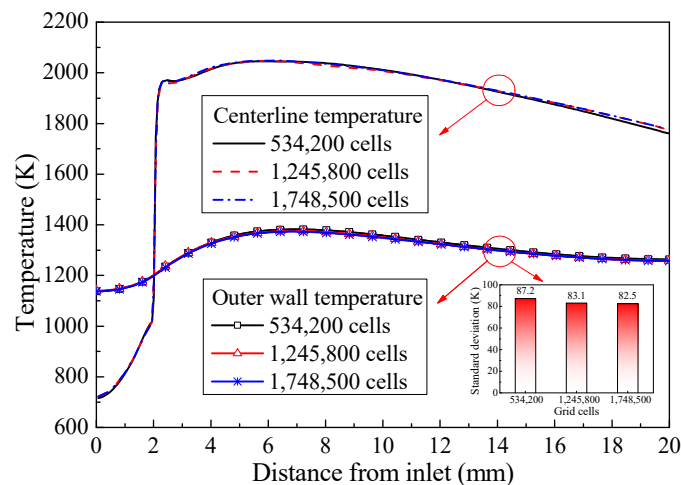


Figure 2. Grid independence study. $D_{\text{in}} = 2 \text{ mm}$, $m_{\text{H}_2} = 2.16 \text{ g/h}$, and $\Phi = 1.0$.

3. Results and Discussion

3.1. Effect of Hydrogen Mass Flow Rate

Figure 3 illustrates the distribution of the mass fraction of the H radical and velocity at the XZ plane in the MCs with different channel diameters D_{in} under various m_{H_2} of 1.08, 2.16, 2.88, and 3.60 g/h where $\Phi = 1.0$. Usually, the H radical can be used as an indicator of the flame front where the reaction zone of the hydrogen flame is located [46]. The velocity level lines were utilized to show the recirculation zones in the swirl MC. It is clearly seen from Figure 3 that this flame type is characterized by the presence of two recirculation zones, where the inner recirculation zone is located on the centerline and the corner recirculation zone is positioned downstream of the swirler exit plane and in the proximity of the inner sidewall of the swirl MC. The flame is anchored by the recirculation zones and the low velocity zones in the vicinity of the recirculation zone, and the anchoring location of the flame root is the starting position of the inner recirculation zone. Indeed, the recirculation zone helps to generate a pool of radicals for combustion reactions, which facilitates flame anchoring. In addition, the recirculation zone increases the residence time of the combustion species, while also preventing the flame root from being blown downstream. The effects of different m_{H_2} and D_{in} in the swirl MC on the flame characteristics can also be evidently observed in Figure 3. The distribution of the H radical is elongated, and the maximum value of H mass fraction also increases with an increase in m_{H_2} . The combustion heat release in the same volume increases with an increasing m_{H_2} , which intensifies the chemical reactions. The flame velocity becomes larger at a high m_{H_2} since the inlet velocity rises.

With regards to the flame root, almost no change was observed when increasing m_{H_2} because the flame root anchoring location still remained at the starting position of the inner recirculation zone. Only the location of the flame tip moved downstream with larger m_{H_2} , which means that the flame extended further downstream. By fixing m_{H_2} to compare and analyze the effect of D_{in} , did we find that a decrease in D_{in} stretched the H radical distribution and increased the maximum value of the H mass fraction. At the same input heat, the small diameter MC had a larger volumetric heat. As a result, the combustion reaction was intensified by reducing the channel diameter. To better show the recirculation zones, Figure 4 shows the flow streamlines at the XZ plane in the swirl MC with different D_{in} where the m_{H_2} was fixed at 2.16 g/h. Both the inner and corner recirculation zones were enlarged due to the larger flow channel diameter. The inner recirculation zone extended approximately 5, 7.5, and 10 mm in the axial direction for the MC with channel diameters of 2, 3, and 4 mm, respectively. Indeed, the channel cross-section was larger at a large channel diameter. In terms of the law of conservation of mass, the velocity became smaller as the channel cross-section became larger. A larger recirculation zone is conducive to increasing the residence time of the reaction species and to form a radical pool for anchoring the flame to the recirculation zone.

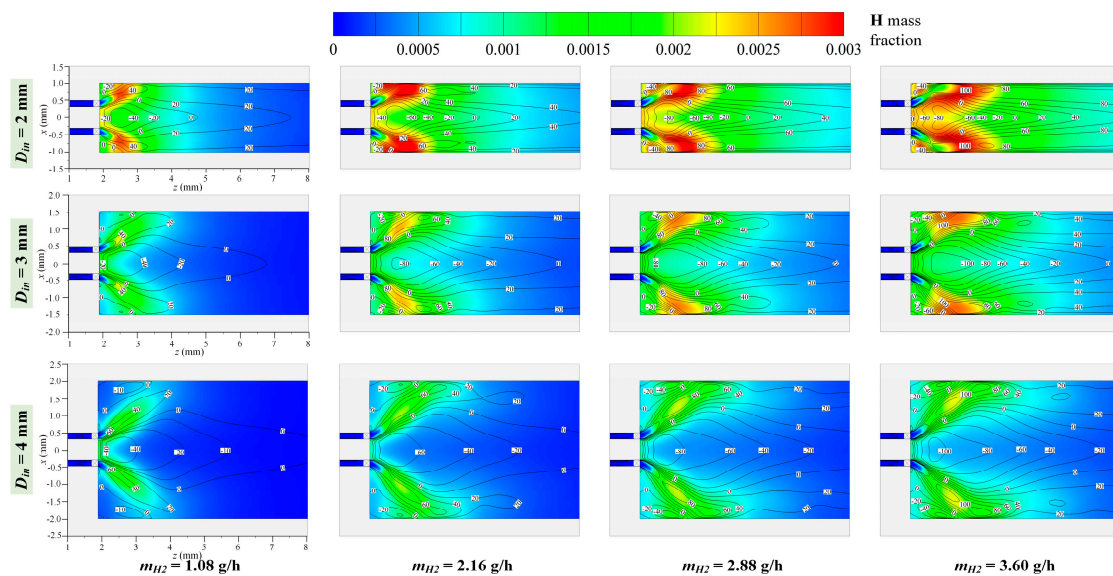


Figure 3. Colored contours of mass fractions of the radical H with overlaid velocity level lines (black line) under various hydrogen mass flow rates at the XZ plane in the swirl MC with different channel diameters.

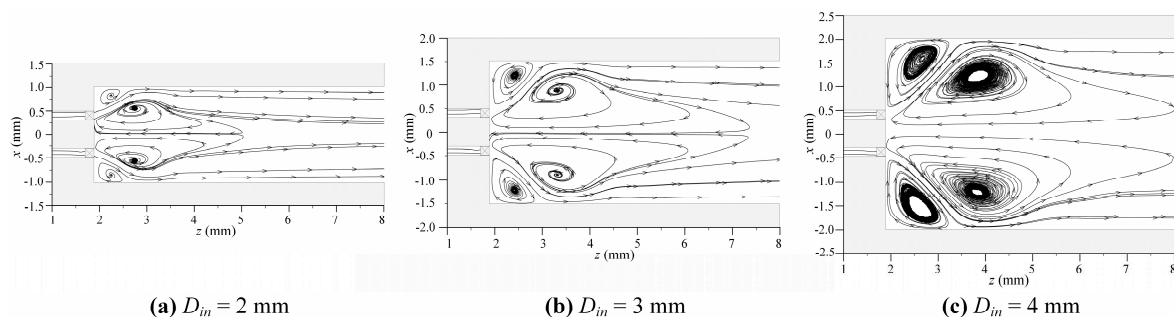


Figure 4. The flow streamlines at the XZ plane in the MC with different channel diameters ($m_{H_2} = 2.16$ g/h).

Combustion efficiency, based on the hydrogen mass fractions at the swirl MC inlet and outlet, is defined by:

$$\eta_c = \left(1 - \frac{\omega_{out}}{\omega_{in}}\right) \times 100\% \quad (10)$$

where η_c is the combustion efficiency, ω_{in} and ω_{out} are the hydrogen mass fractions at the MC inlet and outlet, respectively.

Figure 5 shows the effect of D_{in} on the combustion efficiency under various m_{H_2} . It is clear that combustion efficiency decreased with an increase in m_{H_2} due to the increase of inlet velocity, which resulted in a short residence time of reactants. Meanwhile, a large D_{in} can obviously increase the combustion efficiency. For instance, the combustion efficiency increased from 94.77% to 98.17% when D_{in} rose from 2 mm to 4 mm at $m_{H_2} = 3.60$ g/h. This can be ascribed to the larger recirculation zone, which increased the residence time of reactants. On the other hand, the combustion efficiency in the swirl MC with a large D_{in} is less susceptible to the changes in m_{H_2} , as shown in Figure 5. For example, when m_{H_2} increased from 1.08 g/h to 3.60 g/h, the combustion efficiency of $D_{in} = 2$ mm decreased by 4.56%, while the combustion efficiency of $D_{in} = 4$ mm only decreased by 1.49%.

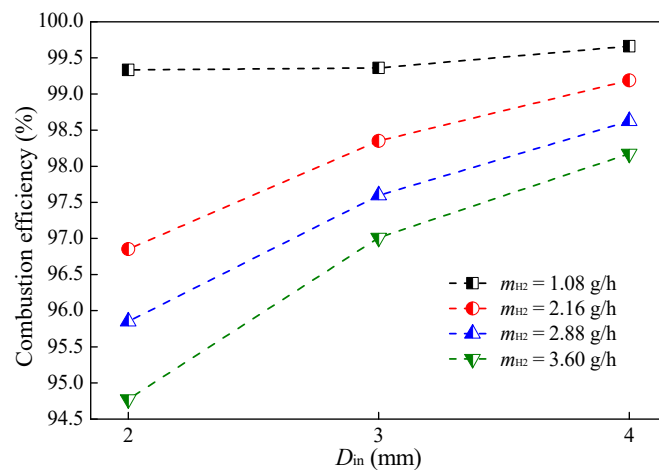


Figure 5. Combustion efficiency under various channel diameters.

As for the outer wall temperature distributions, they are depicted in Figure 6 under different D_{in} and m_{H_2} . At the case of $m_{H_2} = 1.08$ g/h, $D_{in} = 2$ mm had the highest wall temperature distribution along the entire wall. However, with the increase of m_{H_2} , the outer wall temperature near the inlet of the swirl MC with $D_{in} = 2$ mm was obviously lower than the swirl MC with $D_{in} = 4$ mm. This is because there was a corner recirculation zone near the swirler plane and the inner wall of the chamber. The corner recirculation zone was enlarged with an increasing D_{in} , which enhanced heat transfer. Thus, the wall temperature near the inlet increased with a rise in D_{in} .

Figure 7 demonstrates the effect of D_{in} on the average outer wall temperature and standard deviation at different m_{H_2} . Here, the uniformity of wall temperature was assessed by the standard deviation. As for the standard deviation σ_T , it is calculated as:

$$\sigma_T = \sqrt{\frac{\sum_{i=1}^N A_i (T_{w,i} - T_{ave})^2}{\sum_{i=1}^N A_i}} \quad (11)$$

$$T_{ave} = \frac{\sum_{i=1}^N T_{w,i} A_i}{\sum_{i=1}^N A_i} \quad (12)$$

where $T_{w,i}$ and A_i are the outer wall temperature and area of element surface i , respectively; and T_{ave} is the average wall temperature.

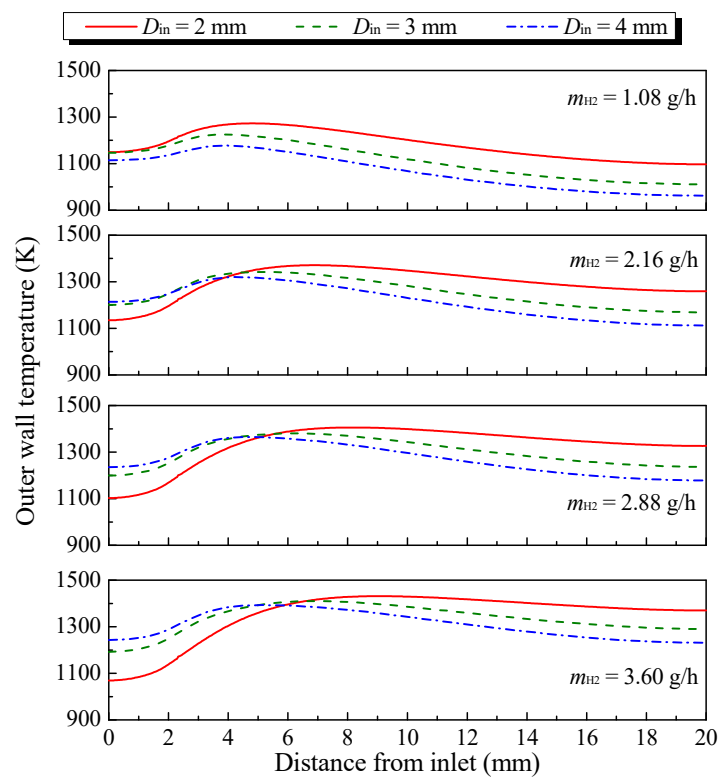


Figure 6. Comparisons of outer wall temperature distributions under different D_{in} and m_{H_2} .

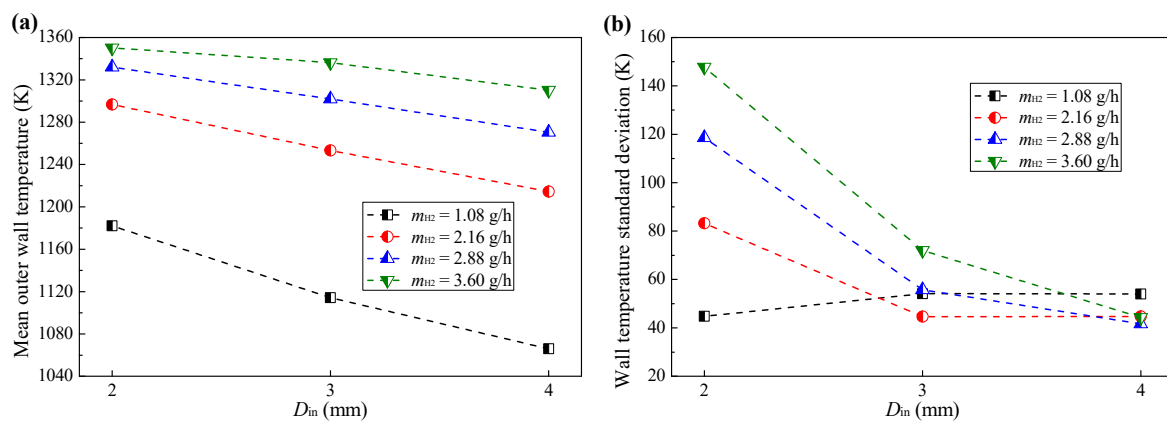


Figure 7. (a) Mean outer wall temperature and (b) temperature standard deviation under different D_{in} and m_{H_2} .

As shown in Figure 7, the MC with $D_{in} = 2$ mm had the largest value of average wall temperature, which is in conformity with the temperature distributions (Figure 6). When m_{H_2} increased from 1.08 g/h to 3.60 g/h, the average wall temperature of the swirl MC with $D_{in} = 2$ mm was 116.2 K, 82.2 K, 61.5 K, and 40.1 K higher than the swirl MC with $D_{in} = 4$ mm, respectively. Nevertheless, the channel diameter D_{in} of 4 mm obtained a very uniform temperature distribution due to the lowest temperature standard deviation. For example, the temperature standard deviations of the swirl MC with $D_{in} = 2, 3,$ and 4 mm were 147.8 K, 72.1 K, and 44.3 K, respectively, where $m_{H_2} = 3.60$ g/h.

The energy output of the MC is of great significance for the micro thermophotovoltaic power generator. The emitter efficiency η_e is calculated by $\eta_e = (Q_0 / m_{H_2} Q_{LHV}) \times 100\%$, where Q_{LHV} is the lower heating value of hydrogen which is 119.96 MJ/kg. Figure 8 shows the emitter efficiency of the MC with various D_{in} at different m_{H_2} . As m_{H_2} becomes larger, the emitter efficiency decreases. The reason is that in the process of increasing m_{H_2} , the heat loss of high-temperature exhaust gas is

larger and the combustion efficiency becomes lower. In addition, the swirl MC with $D_{in} = 4$ mm had the highest emitter efficiency of 65.5% at $m_{H_2} = 1.08$ g/h, while the emitter efficiency of $D_{in} = 2$ mm was only 57.3% at $m_{H_2} = 1.08$ g/h. This is because the radiation surface increased with an increase in D_{in} . When m_{H_2} increased from 1.08 g/h to 3.60 g/h, the emitter efficiency of the swirl MC with $D_{in} = 4$ mm rose by 14.1%, 30.4%, 38.1%, and 45.4%, respectively, compared to the swirl MC with $D_{in} = 2$ mm.

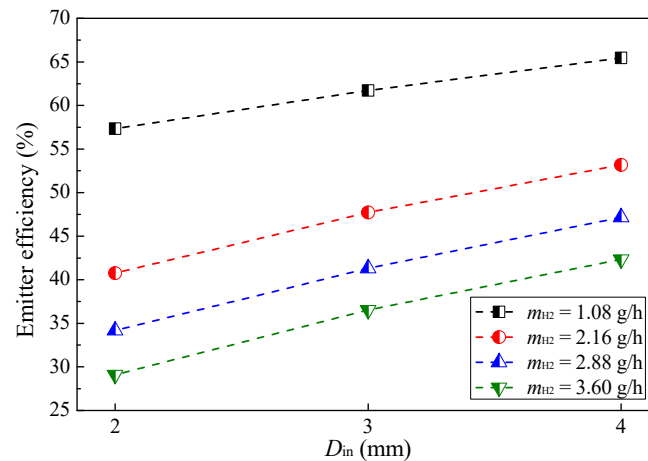


Figure 8. Emitter efficiency under different D_{in} and m_{H_2} .

3.2. Effect of Thermal Conductivity

It is recognized that the thermal conductivity of solid walls is considerably related to the flame characteristics of micro combustion [42,47]. For the purpose of investigating the effect of thermal conductivity, in this section, the density, specific heat, emissivity of solid walls were fixed, just like the silicon carbide. Only the thermal conductivity changed and the values of 0.1, 1.05, 10, 32.8, 50, 100, and 150 were selected to investigate this effect on the combustion and thermal performances. Moreover, m_{H_2} and Φ were fixed at 2.88 g/h and 1.0, respectively.

Figure 9 demonstrates the combustion efficiency in the swirl MC with various D_{in} and thermal conductivities. The combustion efficiency can be significantly improved by increasing thermal conductivity when the thermal conductivity was less than approximately 10 W/m·K. When the thermal conductivity was between 10 W/m·K and 150 W/m·K, the combustion efficiency was almost the same. This phenomenon can be attributed to two reasons. Firstly, as the thermal conductivity rises, the recirculation zone is enlarged, resulting in increasing residence times of reactants. Secondly, a high thermal conductivity enhances both the axial and transversal heat transfers of solid walls in the MC, leading to a better preheating of the incoming fresh reactants. These two reasons can be observed in detail in Figures 10 and 11. The colored contours of mass fraction of the H radical with overlaid flow streamlines (black line) under various thermal conductivities at the XZ plane in the swirl MC with different channel diameters are depicted in Figure 10. It can be clearly observed that increasing thermal conductivity can increase the length of the inner recirculation zone. This is due to the stronger volumetric expansion effect of the gas caused by the better preheating at larger thermal conductivity [47]. These larger recirculation zones increase the residence time of burned gas and the convection time between high-temperature gas and solid walls. In terms of the H radical, the maximum value of the H radical increases with the increase of thermal conductivity, and the reactive zone is slightly elongated, which means that increasing the thermal conductivity of solid walls can intensify combustion chemical reactions. This is because upstream fresh reactants are preferably preheated by downstream high-temperature combustion products with higher thermal conductivity as a result of better heat recirculation caused by solid walls. As shown by the temperature contours in Figure 11, the high-temperature region moved upstream with an increasing thermal conductivity. This means that the chemical reaction zone moved toward the combustor inlet. Moreover, the temperature of

the entrance section with high thermal conductivity was obviously greater. Higher temperatures can increase the temperature of incoming fresh reactants, which in turn raises the chemical reaction rates.

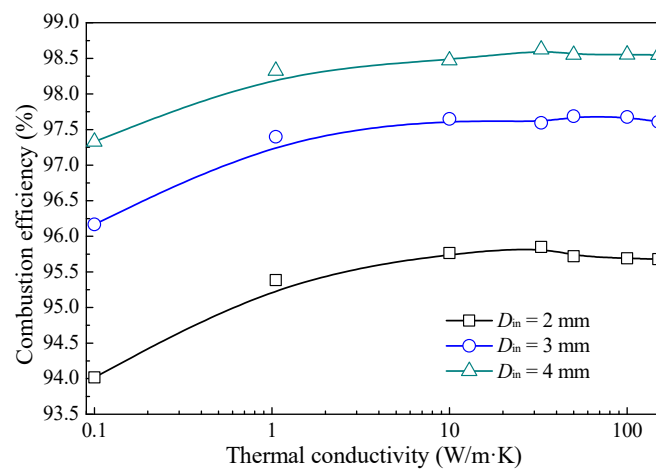


Figure 9. Combustion efficiency under various thermal conductivities.

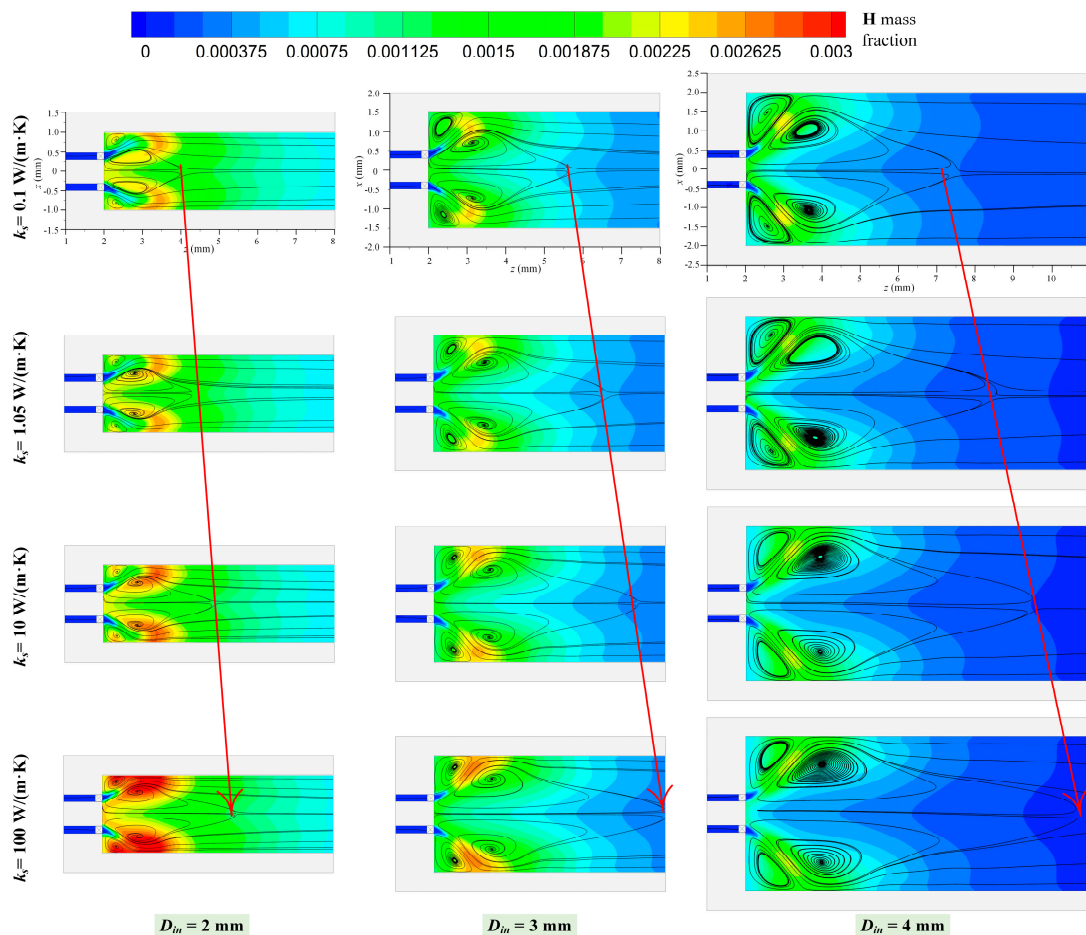


Figure 10. Colored contours of mass fractions of the H radical with overlaid flow streamlines (black line) under various thermal conductivities at the XZ plane in the swirl MC with different channel diameters.

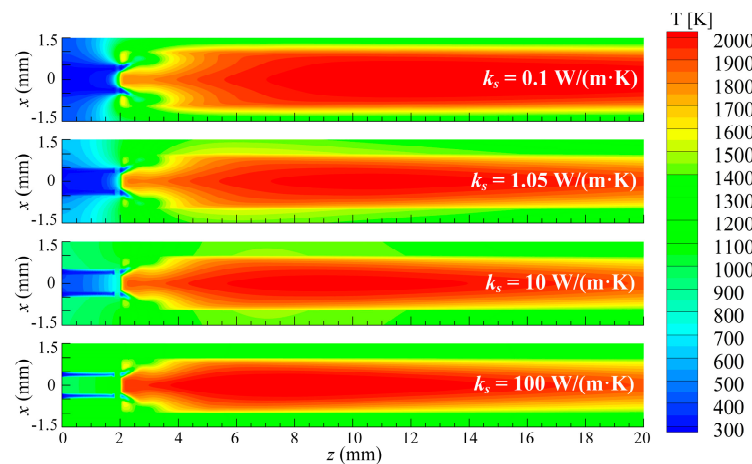


Figure 11. Temperature contours under various thermal conductivities at the XZ plane in the swirl MC with $D_{in} = 2$ mm.

Figure 12 illustrates the temperature distributions, average wall temperature, and temperature standard deviation of the outer wall, as well as the emitter efficiency of the MC under various thermal conductivities. As a result of the suppressed heat transfer of walls with high thermal resistance, it is known from Figure 12a that the MC with the thermal conductivity of 0.1 W/m·K obtained the lowest wall temperature. In addition, the outer wall temperature near the inlet obviously increased with an increasing thermal conductivity, which is beneficial for preheating the upstream reactants. Raising the thermal conductivity makes the outer wall temperature more uniform, which is beneficial for the micro thermophotovoltaic power generators. Figure 12b,c demonstrate the mean value and standard deviation of the outer wall temperature with different thermal conductivities. The average temperature of the outer wall was remarkably improved by increasing thermal conductivity when the thermal conductivity was less than approximately 32.8 W/m·K. When thermal conductivity increased from 32.8 W/m·K to 150 W/m·K, the change in mean outer wall temperature was almost negligible. This means that there is a critical point of thermal conductivity that can increase the wall temperature. When thermal conductivity exceeds the critical point, continuing to increase the thermal conductivity has a negligible effect on the wall temperature level. Nevertheless, the temperature standard deviation was decreasing with increasing thermal conductivity, as presented in Figure 12c. For example, when thermal conductivity rises from 0.1 W/m·K to 150 W/m·K, the temperature standard deviation of $D_{in} = 2$ mm is reduced from 292.8 K to 47.9 K, and the temperature standard deviation of $D_{in} = 4$ mm is reduced from 169.7 K to 15.1 K. Moreover, the difference in temperature standard deviation of MC with different D_{in} is small at a large thermal conductivity. The effect of thermal conductivity on emitter efficiency is illustrated in Figure 12d. Just like the mean outer wall temperature, an increase in thermal conductivity results in a significant rise in emitter efficiency when the thermal conductivity is less than approximately 10 W/m·K. Whereas, when thermal conductivity exceeds approximately 10 W/m·K, increasing it does not increase the emitter efficiency. For instance, in the case of $m_{H_2} = 2.88$ g/h, the maximum emitter efficiencies of the MCs with $D_{in} = 2, 3,$ and 4 mm were about 34.0%, 41.3%, and 46.9%, respectively, when only the thermal conductivity was changed.

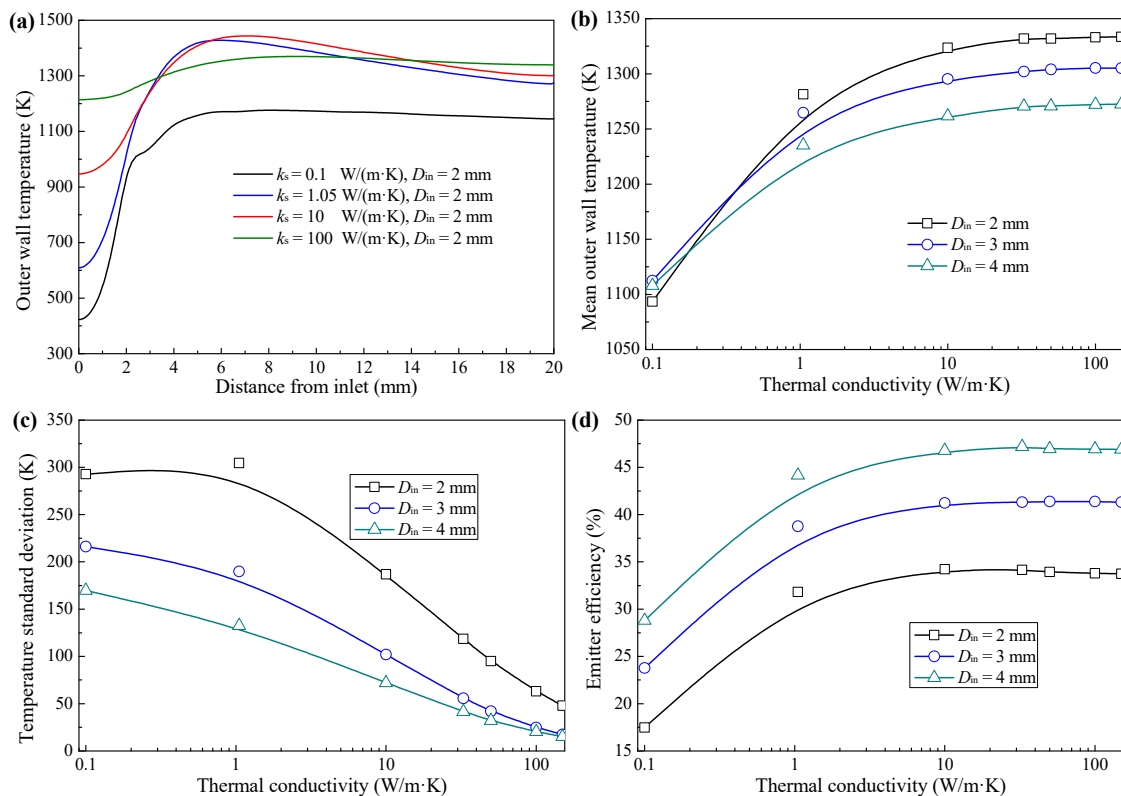


Figure 12. Effect of thermal conductivity on (a) temperature distributions of the outer wall, (b) mean temperature of the outer wall, (c) temperature standard deviation, and (d) emitter efficiency.

3.3. Effect of Preferential Transport

It is recognized that the local equivalence ratio near the flame front can be changed by the different mass diffusivities of reactant species, known as preferential transport effect [46,48,49]. The local equivalence ratio ϕ_{local} is calculated from the fuel/oxygen atom balance, using eight major species from the detailed H_2/air chemical reaction mechanism (H_2 , O_2 , O , H , OH , H_2O , HO_2 , and H_2O_2).

$$\phi_{\text{local}} = \frac{0.5(X_{\text{H}_2} + X_{\text{H}_2\text{O}} + X_{\text{H}_2\text{O}_2}) + 0.25(X_{\text{H}} + X_{\text{OH}} + X_{\text{HO}_2})}{0.5(X_{\text{O}} + X_{\text{OH}} + X_{\text{H}_2\text{O}}) + (X_{\text{O}_2} + X_{\text{H}_2\text{O}_2} + X_{\text{HO}_2})} \quad (13)$$

where X is the mole fraction of species.

Figures 13 and 14 demonstrate the contours of $\phi_{\text{local}} - \phi_{\text{inlet}}$ and flow streamlines at the XZ plane in the swirl MC. Figure 13a shows the effect of the hydrogen mass flow rate where the channel diameter of the swirl MC is 2 mm; Figure 13b shows the effect of thermal conductivity where the channel diameter of the swirl MC was 2 mm and the hydrogen mass flow rate was 2.88 g/h; Figure 14 is given to compare the effect of the channel diameter on the local equivalence ratio, where the hydrogen mass flow rate was 2.88 g/h. As depicted in Figure 13, increases in the hydrogen mass flow rate and thermal conductivity extended the inner recirculation zone; this can result in an increase in the proportion of the larger local equivalence ratio area in the recirculation zone. It is shown in Figure 14 that the region with a larger local equivalence ratio still remains the starting location of recirculation zone when the channel diameter of the swirl MC changes. It can obviously be seen that the larger local equivalence ratio is located in the inner and corner recirculation zones, where the flame root anchors. There is a peak local equivalence ratio on both sides of the swirler exit, mainly due to the sudden expansion at the swirler exit resulting in sharp velocity gradients. Katta and Roquemore [50] confirmed that sharp velocity gradients contribute to the preferential diffusion effect. The region with a large local equivalence ratio due to the preferential diffusion effect is beneficial to the chemical reaction and flame stability.

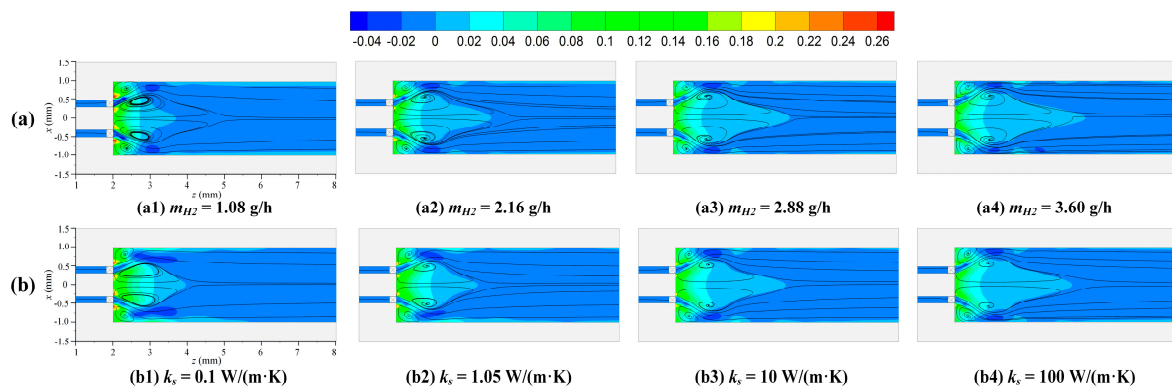


Figure 13. Contours of $\phi_{\text{local}} - \phi_{\text{inlet}}$ with overlaid flow streamlines (black line) for different hydrogen mass flow rates and thermal conductivities at the XZ plane in the swirl MC: (a) effect of hydrogen mass flow rate, where $D_{\text{in}} = 2$ mm; (b) effect of thermal conductivity, where $D_{\text{in}} = 2$ mm and $m_{\text{H}_2} = 2.88$ g/h.

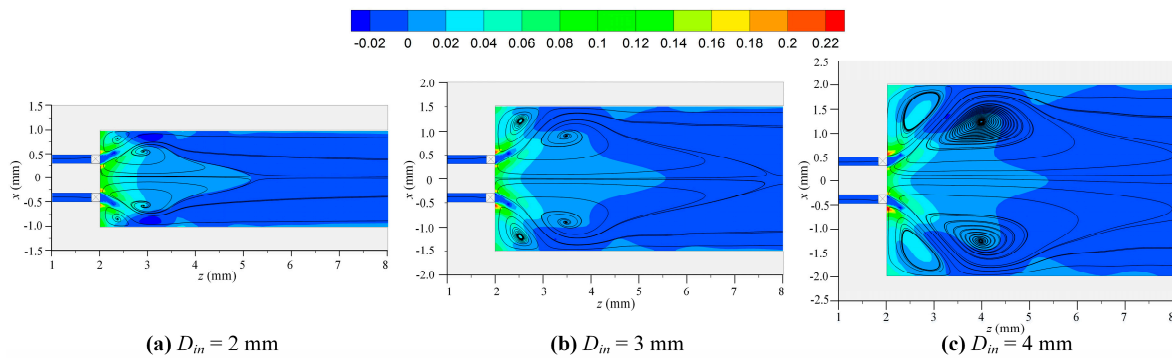


Figure 14. Contours of $\phi_{\text{local}} - \phi_{\text{inlet}}$ with overlaid flow streamlines (black line) at the XZ plane in the swirl MC under various channel diameters ($m_{\text{H}_2} = 2.88$ g/h).

4. Conclusions

The effects of channel diameter on the combustion and thermal behavior under various H_2/air mass flow rates and thermal conductivities in a swirl MC were examined numerically. We established a three-dimensional numerical model with a detailed hydrogen/air chemical reaction mechanism to analyze these characteristics. The main conclusions are summarized as follows:

- (1) The formation of inner and corner recirculation zones with low local velocities in the swirl MC was due to the swirling flow facilitating flame anchoring;
- (2) The local equivalence ratio was larger in the recirculation zones, which confirms that the recirculation zones helped to create a radical pool, thereby anchoring the flame to there;
- (3) Although parameters such as channel diameter, inlet mass flow rate, and thermal conductivity of the solid wall changed, the flame root was firmly anchored to the starting position of the recirculation zones;
- (4) The combustion intensity was stronger in the MC with a small D_{in} of 2 mm, which had a higher wall temperature. But, a more uniform wall temperature and a larger emitter efficiency was obtained in the MC with $D_{\text{in}} = 4$ mm;
- (5) Increasing the thermal conductivity enhanced the thermal performance of the combustion efficiency and emitter efficiency when the thermal conductivity was no greater than approximately 10 W/m·K because of the better preheating and heat transfer performances;
- (6) There was a critical point of thermal conductivity (approximately between 10 and 30 W/m·K) that can increase the thermal performance of an MC. When thermal conductivity exceeds the critical thermal conductivity, continuing to increase thermal conductivity has a negligible impact

on thermal performance. Nevertheless, the wall temperature standard deviation decreases with increasing thermal conductivity.

Author Contributions: Conceptualization, X.Y.; methodology, X.Y.; software, X.Y.; validation, X.Y.; investigation, X.Y.; data analysis, X.Y.; writing—original draft preparation, X.Y.; writing—review and editing, X.Y., Z.H., L.Z., S.D. and H.T.; supervision, S.D. and H.T.

Funding: This research was funded by the National Natural Science Foundation of China, grant number 51576054 and the China Scholarship Council, grant number 201906120194.

Acknowledgments: X.Y. wishes to express his gratitude to Ms. Chen Yan for her extraordinary patience and consistent encouragement.

Conflicts of Interest: The authors declare no conflict of interest.

References

- Hosseini, S.E. Micro-power generation using micro-turbine (moving) and thermophotovoltaic (non-moving) systems. *Proc. Inst. Mech. Eng. Part A J. Power Energy* **2019**, *233*. [[CrossRef](#)]
- Ju, Y.; Maruta, K. Microscale combustion: Technology development and fundamental research. *Prog. Energy Combust. Sci.* **2011**, *37*, 669–715. [[CrossRef](#)]
- Chou, S.K.; Yang, W.M.; Chua, K.J.; Li, J.; Zhang, K.L. Development of micro power generators—A review. *Appl. Energy* **2011**, *88*, 1–16. [[CrossRef](#)]
- Burugupally, S.; Weiss, L. Power Generation via Small Length Scale Thermo-Mechanical Systems: Current Status and Challenges, a Review. *Energies* **2018**, *11*, 2253. [[CrossRef](#)]
- Waitz, I.A.; Gauba, G.; Tzeng, Y.S. Combustors for micro-gas turbine engines. *J. Fluids Eng.* **1998**, *12*, 109–117. [[CrossRef](#)]
- Mehra, A.; Zhang, X.; Ayon, A.A.; Waitz, I.A.; Spadaccini, C.M. A six-wafer combustion system for a silicon micro gas turbine engine. *J. Microelectromech. Syst.* **2000**, *9*, 517–527. [[CrossRef](#)]
- Yang, W.M.; Jiang, D.Y.; Chou, S.K.; Chua, K.J.; Karthikeyan, K.; An, H. Experimental study on micro modular combustor for micro-thermophotovoltaic system application. *Int. J. Hydrogen Energy* **2012**, *37*, 9576–9583. [[CrossRef](#)]
- Yang, W.M.; Chou, S.K.; Shu, C.; Xue, H.; Li, Z.W.; Li, D.T.; Pan, J.F. Microscale combustion research for application to micro thermophotovoltaic systems. *Energy Convers. Manag.* **2003**, *44*, 2625–2634. [[CrossRef](#)]
- Li, Y.-H.; Hong, J.R. Power generation performance of hydrogen-fueled micro thermophotovoltaic reactor. *Int. J. Hydrogen Energy* **2018**, *43*, 1459–1469. [[CrossRef](#)]
- Yang, W.M.; Chou, S.K.; Shu, C.; Li, Z.W.; Xue, H. A prototype microthermophotovoltaic power generator. *Appl. Phys. Lett.* **2004**, *84*, 3864–3866. [[CrossRef](#)]
- Yang, W.; Chou, S.; Shu, C.; Xue, H.; Li, Z. Effect of wall thickness of micro-combustor on the performance of micro-thermophotovoltaic power generators. *Sens. Actuators A Phys.* **2005**, *119*, 441–445.
- Yan, J.; Liao, X.; Yan, D.; Chen, Y. Review of Micro Thermoelectric Generator. *J. Microelectromech. Syst.* **2018**, *27*, 1–18. [[CrossRef](#)]
- Yadav, S.; Sharma, P.; Yamasani, P.; Minaev, S.; Kumar, S. A prototype micro-thermoelectric power generator for micro-electromechanical systems. *Appl. Phys. Lett.* **2014**, *104*, 123903. [[CrossRef](#)]
- Aravind, B.; Raghuram, G.K.S.; Kishore, V.R.; Kumar, S. Compact design of planar stepped micro combustor for portable thermoelectric power generation. *Energy Convers. Manag.* **2018**, *156*, 224–234. [[CrossRef](#)]
- Hosseini, S.; Owens, E.; Krohn, J.; Lylek, J. Experimental investigation into the effects of thermal recuperation on the combustion characteristics of a non-premixed meso-scale vortex combustor. *Energies* **2018**, *11*, 3390. [[CrossRef](#)]
- Wan, J.; Fan, A.; Maruta, K.; Yao, H.; Liu, W. Experimental and numerical investigation on combustion characteristics of premixed hydrogen/air flame in a micro-combustor with a bluff body. *Int. J. Hydrogen Energy* **2012**, *37*, 19190–19197. [[CrossRef](#)]
- Wan, J.; Fan, A.; Yao, H.; Liu, W. Experimental investigation and numerical analysis on the blow-off limits of premixed CH₄/air flames in a mesoscale bluff-body combustor. *Energy* **2016**, *113*, 193–203. [[CrossRef](#)]
- Bagheri, G.; Hosseini, S.E.; Wahid, M.A. Effects of bluff body shape on the flame stability in premixed micro-combustion of hydrogen–air mixture. *Appl. Therm. Eng.* **2014**, *67*, 266–272. [[CrossRef](#)]

19. Hosseini, S.E.; Wahid, M.A. Investigation of bluff-body micro-flameless combustion. *Energy Convers. Manag.* **2014**, *88*, 120–128. [[CrossRef](#)]
20. Lloyd, S.A.; Weinberg, F.J. A burner for mixtures of very low heat content. *Nature* **1974**, *251*, 47–49. [[CrossRef](#)]
21. Kim, N.; Kato, S.; Kataoka, T.; Yokomori, T.; Maruyama, S.; Fujimori, T.; Maruta, K. Flame stabilization and emission of small Swiss-roll combustors as heaters. *Combust. Flame* **2005**, *141*, 229–240. [[CrossRef](#)]
22. Wang, W.; Zuo, Z.; Liu, J. Numerical study of the premixed propane/air flame characteristics in a partially filled micro porous combustor. *Energy* **2019**, *167*, 902–911. [[CrossRef](#)]
23. Li, J.; Li, Q.; Wang, Y.; Guo, Z.; Liu, X. Fundamental flame characteristics of premixed H₂-air combustion in a planar porous micro-combustor. *Chem. Eng. J.* **2016**, *283*, 1187–1196. [[CrossRef](#)]
24. Marbach, T.L.; Sadasivuni, V.; Agrawal, A.K. Investigation of a Miniature Combustor Using Porous Media Surface Stabilized Flame. *Combust. Sci. Technol.* **2007**, *179*, 1901–1922. [[CrossRef](#)]
25. Mikami, M.; Maeda, Y.; Matsui, K.; Seo, T.; Yuliati, L. Combustion of gaseous and liquid fuels in meso-scale tubes with wire mesh. *Proc. Combust. Inst.* **2013**, *34*, 3387–3394. [[CrossRef](#)]
26. Yang, W.M.; Chua, K.J.; Pan, J.F.; Jiang, D.Y.; An, H. Development of micro-thermophotovoltaic power generator with heat recuperation. *Energy Convers. Manag.* **2014**, *78*, 81–87. [[CrossRef](#)]
27. Tang, A.; Cai, T.; Deng, J.; Xu, Y.; Pan, J. Experimental investigation on combustion characteristics of premixed propane/air in a micro-planar heat recirculation combustor. *Energy Convers. Manag.* **2017**, *152*, 65–71. [[CrossRef](#)]
28. Alipoor, A.; Saidi, M.H. Numerical study of hydrogen-air combustion characteristics in a novel micro-thermophotovoltaic power generator. *Appl. Energy* **2017**, *199*, 382–399. [[CrossRef](#)]
29. Chou, S.K.; Yang, W.M.; Li, J.; Li, Z.W. Porous media combustion for micro thermophotovoltaic system applications. *Appl. Energy* **2010**, *87*, 2862–2867. [[CrossRef](#)]
30. Akhtar, S.; Khan, M.N.; Kurnia, J.C.; Shamim, T. Investigation of energy conversion and flame stability in a curved micro-combustor for thermo-photovoltaic (TPV) applications. *Appl. Energy* **2017**, *192*, 134–145. [[CrossRef](#)]
31. Yang, X.; He, Z.; Dong, S.; Tan, H. Enhancement of thermal performance by converging-diverging channel in a micro tube combustor fueled by premixed hydrogen/air. *Int. J. Hydrogen Energy* **2019**, *44*, 1213–1226. [[CrossRef](#)]
32. Tang, A.; Pan, J.; Yang, W.; Xu, Y.; Hou, Z. Numerical study of premixed hydrogen/air combustion in a micro planar combustor with parallel separating plates. *Int. J. Hydrogen Energy* **2015**, *40*, 2396–2403. [[CrossRef](#)]
33. Amani, E.; Alizadeh, P.; Moghadam, R.S. Micro-combustor performance enhancement by hydrogen addition in a combined baffle-bluff configuration. *Int. J. Hydrogen Energy* **2018**, *43*, 8127–8138. [[CrossRef](#)]
34. Tang, A.; Xu, Y.; Pan, J.; Yang, W.; Jiang, D.; Lu, Q. Combustion characteristics and performance evaluation of premixed methane/air with hydrogen addition in a micro-planar combustor. *Chem. Eng. Sci.* **2015**, *131*, 235–242. [[CrossRef](#)]
35. Yang, W.M.; Chou, S.K.; Shu, C.; Li, Z.W.; Xue, H. Research on micro-thermophotovoltaic power generators. *Sol. Energy Mater. Sol. Cells* **2003**, *80*, 95–104. [[CrossRef](#)]
36. Lee, S.I.; Um, D.H.; Kwon, O.C. Performance of a micro-thermophotovoltaic power system using an ammonia-hydrogen blend-fueled micro-emitter. *Int. J. Hydrogen Energy* **2013**, *38*, 9330–9342. [[CrossRef](#)]
37. Nadimi, E.; Jafarmadar, S. The numerical study of the energy and exergy efficiencies of the micro-combustor by the internal micro-fin for thermophotovoltaic systems. *J. Clean. Prod.* **2019**, *235*, 394–403. [[CrossRef](#)]
38. Gentillon, P.; Singh, S.; Lakshman, S.; Zhang, Z.; Paduthol, A.; Ekins-Daukes, N.J.; Chan, Q.N.; Taylor, R.A. A comprehensive experimental characterisation of a novel porous media combustion-based thermophotovoltaic system with controlled emission. *Appl. Energy* **2019**, *254*, 113721. [[CrossRef](#)]
39. Yang, X.; Zhao, L.; He, Z.; Dong, S.; Tan, H. Comparative study of combustion and thermal performance in a swirling micro combustor under premixed and non-premixed modes. *Appl. Therm. Eng.* **2019**, *160*, 114110. [[CrossRef](#)]
40. Yang, X.; He, Z.; Niu, Q.; Dong, S.; Tan, H. Numerical analysis of turbulence radiation interaction effect on radiative heat transfer in a swirling oxyfuel furnace. *Int. J. Heat Mass Transf.* **2019**, *141*, 1227–1237. [[CrossRef](#)]
41. Ali Beskok, G.E.K. A model for flows in channels, pipes, and ducts at micro and nano scales. *Microscale Thermophys. Eng.* **1999**, *3*, 43–77. [[CrossRef](#)]
42. Norton, D.G.; Vlachos, D.G. A CFD study of propane/air microflame stability. *Combust. Flame* **2004**, *138*, 97–107. [[CrossRef](#)]

43. Norton, D.G.; Vlachos, D.G. Combustion characteristics and flame stability at the microscale: A CFD study of premixed methane/air mixtures. *Chem. Eng. Sci.* **2003**, *58*, 4871–4882. [[CrossRef](#)]
44. Yan, Y.; Xu, F.; Xu, Q.; Zhang, L.; Yang, Z.; Ran, J. Influence of controllable slit width and angle of controllable flow on hydrogen/air premixed combustion characteristics in micro combustor with both sides-slitted bluff body. *Int. J. Hydrogen Energy* **2019**, *44*, 20482–20492. [[CrossRef](#)]
45. Li, J.; Chou, S.K.; Li, Z.W.; Yang, W.M. A comparative study of H₂-air premixed flame in micro combustors with different physical and boundary conditions. *Combust. Theory Model.* **2008**, *12*, 325–347. [[CrossRef](#)]
46. Wan, J.; Fan, A.; Yao, H.; Liu, W. Flame-anchoring mechanisms of a micro cavity-combustor for premixed H₂/air flame. *Chem. Eng. J.* **2015**, *275*, 17–26. [[CrossRef](#)]
47. Wan, J.; Fan, A.; Yao, H.; Liu, W. Effect of thermal conductivity of solid wall on combustion efficiency of a micro-combustor with cavities. *Energy Convers. Manag.* **2015**, *96*, 605–612. [[CrossRef](#)]
48. Barlow, R.S.; Dunn, M.J.; Magnotti, G. Preferential transport effects in premixed bluff-body stabilized CH₄/H₂ flames. *Combust. Flame* **2015**, *162*, 727–735. [[CrossRef](#)]
49. Barlow, R.S.; Dunn, M.J.; Sweeney, M.S.; Hochgreb, S. Effects of preferential transport in turbulent bluff-body-stabilized lean premixed CH₄/air flames. *Combust. Flame* **2012**, *159*, 2563–2575. [[CrossRef](#)]
50. Katta, V.; Roquemore, W.M. C/H atom ratio in recirculation-zone-supported premixed and nonpremixed flames. *Proc. Combust. Inst.* **2013**, *34*, 1101–1108. [[CrossRef](#)]



© 2019 by the authors. Licensee MDPI, Basel, Switzerland. This article is an open access article distributed under the terms and conditions of the Creative Commons Attribution (CC BY) license (<http://creativecommons.org/licenses/by/4.0/>).